





## Application of Non-Linear Noise Regression in the Virgo Detector

R. WEIZMANN KIENDREBEOGO <sup>1,2,3,4</sup> MUHAMMED SALEEM <sup>5,3</sup> MARIE ANNE BIZOUARD <sup>2</sup> ANDY H.Y. CHEN <sup>6</sup>  
NELSON CHRISTENSEN <sup>2</sup> CHIA-JUI CHOU <sup>7</sup> MICHAEL W. COUGHLIN <sup>3</sup> KAMIEL JANSSENS <sup>8,9,10</sup>  
S. ZACHARIE KAM <sup>1</sup> JEAN KOULIDIATI <sup>1</sup> AND SHU-WEI YEH<sup>11</sup>

<sup>1</sup>*Laboratoire de Physique et de Chimie de l'Environnement, Université Joseph KI-ZERBO, Ouagadougou, Burkina Faso*

<sup>2</sup>*Artemis, Observatoire de la Côte d'Azur, Université Côte d'Azur, Boulevard de l'Observatoire, F-06304 Nice, France*

<sup>3</sup>*School of Physics and Astronomy, University of Minnesota, Minneapolis, MN 55455, USA*

<sup>4</sup>*IRFU, CEA, Université Paris-Saclay, F-91191 Gif-sur-Yvette, France*

<sup>5</sup>*Center for Gravitational Physics, University of Texas at Austin, Austin, TX 78712, USA*

<sup>6</sup>*Institute of Physics, National Yang-Ming Chiao Tung University, Hsinchu, Taiwan*

<sup>7</sup>*Department of Electrophysics, National Yang Ming Chiao Tung University, Hsinchu, Taiwan*

<sup>8</sup>*Universiteit Antwerpen, Prinsstraat 13, 2000 Antwerpen, Belgium*

<sup>9</sup>*Department of Physics, The University of Adelaide, Adelaide, SA 5005, Australia*

<sup>10</sup>*ARC Centre of Excellence for Dark Matter Particle Physics, Melbourne, Australia*

<sup>11</sup>*Department of Physics, National Tsing Hua University, Hsinchu, Taiwan*

### ABSTRACT

Since the first detection of gravitational waves (GWs) in 2015, the International Gravitational-wave Network has made substantial strides in improving the sensitivity of ground-based detectors. Despite these advancements, many GW signals remain below the detection threshold due to environmental noise that limits sensitivity. In recent years, algorithms such as **DeepClean** have been developed to estimate and remove contamination from various noise sources, addressing linear, non-linear, and non-stationary coupling mechanisms. In this paper, we present noise reduction in the Virgo detector using **DeepClean**, serving as a preliminary step toward integrating Virgo into the online noise reduction pipeline for the O5 observing run. Our results demonstrate the applicability of **DeepClean** in Virgo O3b data, where noise was reconstructed from a total of 225 auxiliary witness channels. These channels were divided into 13 subsets, each corresponding to a specific frequency band, with training and subtraction performed layer-wise in a sequential manner. We observe that the subtraction improves the binary neutron star inspiral range by up to 1.3 Mpc, representing an approximately 2.5% increase. To ensure robust validation, we conduct an injection study with binary black hole waveforms. Matched-filter analyses of the injections showed an average improvement of 1.7% in the recovered SNR, while parameter estimation confirmed that **DeepClean** introduces no bias in the recovered parameters. The successful demonstration provides a pathway for online non-linear noise subtraction in Virgo in the future observing runs.

### 1. INTRODUCTION

Gravitational-wave (GW) events, such as GW150914 (Abbott et al. 2016), GW170817 (Abbott et al. 2017), GW190425 (Abbott et al. 2020b), and GW200105 (Abbott et al. 2020b), among others, have significantly improved our understanding of compact binary mergers (Abbott et al. 2021a, 2023). However, many poten-

tial GW signals remain undetected just below the noise floor, awaiting the successful mitigation of environmental noise sources. In the absence of a GW, the detectors may show fluctuations due to various factors that contribute to the noise of the system, including fundamental, technical, and environmental sources. These noise sources contribute with different and time-varying characteristics in amplitude and frequency. The characterization of the various noise components is crucial to understanding and improving the performance of a detector, in particular when identifying authentic GW signals (Acernese et al. 2023a; Buikema et al. 2020). Fun-

weizmann.kiendrebeogo@oca.eu

muhammed.cholayil@austin.utexas.edu

damental noise includes inherent limitations of detector design materials and quantum mechanics. Thermal noise in the mirror coatings is a fundamental noise in the frequency band of approximately 60-300 Hz. Environmental noise covers external influences like *seismic noise*, *atmospheric noise*, *external thermal fluctuations*, and *Newtonian noise* (Martynov et al. 2016). Technical noise comes from the design and operational aspects of the detector.

The various noise sources make it difficult to clearly discern GW signals, mitigating or subtracting noise within the detectors may expose these missed signals to detection algorithms. To potentially reveal new signals or otherwise improve the signal-to-noise ratio (SNR) of known ones, both the Laser Interferometer GW Observatory (Advanced LIGO; LSC et al. 2015) and Advanced Virgo (Acernese et al. 2014) record several thousands of witness channels (probes and sensors) (Allocca et al. 2020a; Acernese et al. 2023a). These witness channels independently are sensitive to noise from various sources. Some of them collect data to characterize environmental noise sources that couple with the GW readout channel and could therefore be used to subtract noise sources. Only non-fundamental noise can be subtracted. Thus, we prioritize mitigating measurable environmental and technical noise. Through the classification of noise into removable and non-removable categories, our objective is to enhance the sensitivity of GW detectors, ensuring a clearer distinction between real GW signals and noise artifacts.

In the past, some noise subtraction methods, such as Wiener filtering, widely used to subtract linearly coupled noise sources, can face challenges in the presence of *non-stationary* noise (Davis et al. 2019). Furthermore, *non-linear* noise, arising from systems in which the output is not directly proportional to the input, creates complex and unpredictable noise patterns. This non-linearity can be due to a multitude of factors, including complex physical processes within the detector or environmental influences (Driggers et al. 2019). While *non-linear* noise reflects a non-proportional relationship, *non-stationary* noise refers instead to time-dependent variations in an otherwise linear system (Vajente et al. 2020). On the other hand, *non-stationary* noise is characterized by its statistical properties that change over time, adding a layer of complexity to data analysis and signal processing. The dynamic variability of the noise makes it particularly challenging to model and subtract from the data.

At present, there are several narrow-band and broad-band frequency ranges where the sensitivity is significantly made worse than that expected by the design.

Low-frequency (typically around 10-100 Hz) sensitivity is particularly important for many reasons (Ormiston et al. 2020; Vajente et al. 2020). These include the possible detections of high-mass binary mergers at low frequencies, stochastic GW background detection which significantly benefits from the excess GW power in low-frequencies (Christensen 2018; Abbott et al. 2021b), and the pre-merger detectability of Binary Neutron star (BNS) mergers (Abbott et al. 2017) as it allows us to anticipate potential electromagnetic (EM) counterparts (Petrov et al. 2022; Kiendrebeogo et al. 2023). Furthermore, many GW signals that are hidden in noise, would become detectable when noise is adequately minimized in any frequency band.

Much noise is caused by the presence of various environmental and technical noise contributions. It is possible that their sources might have already been being tracked by one or more of the witness sensors. Identifying the appropriate witness channels is a challenging task, which is often done by the experimentalist’s intuition. There are also algorithmic approaches being developed for this purpose, which will be subject of a future paper.

**DeepClean** is a deep-learning infrastructure developed to denoise the GWs strain data using witness channels (Ormiston et al. 2020; Saleem et al. 2023). It has a 1D Convolutional Neural Network (CNN) architecture, with the time-series data from multiple witness sensors as inputs and a single noise prediction as the output. Due to its complex architecture, **DeepClean** is capable of subtracting *non-linear* and *non-stationary* noise from the GW data. The performance of **DeepClean** on LIGO detectors has already been demonstrated in detail in the aforementioned publications (Ormiston et al. 2020; Saleem et al. 2023).

In this work, we focus on the Virgo detector, where some EM noise comes from electrical sources, reaching their peak at the 50 Hz power line frequency. This electrical noise induces modulations in the main GW signal, leading to the generation of symmetric sidebands around 50 Hz. During O3, a feed-forward loop process was used to remove the Virgo mains and its associated sidebands (Allocca et al. 2020b). We also aim to demonstrate the flexibility of the architecture in to be applicable on detectors with different designs. In addition, in this work, we also demonstrate a multi-layer multi-band training approach (simply known as *multi-training*) unlike the subtractions done in Saleem et al. (2023) which were done for a single frequency band with a single layer of training.

In Sec. 2, we describe the methodology implemented in the **DeepClean** algorithm, focusing on noise estimation

and reduction using witness channels. Sec. 3 gives a discussion of the application of **DeepClean** on Virgo’s O3b (the second part of the third observing run of LIGO-Virgo collaboration) data, including the training process and noise subtraction. The results, including analyses of individual frequency bands and the multi-training approach, are presented in Sec. 4. Our conclusion and future prospects are summarized in Sec. 5.

## 2. NOISE SUBTRACTION IN GRAVITATIONAL WAVE DATA

### 2.1. Popular subtraction techniques

Effective noise reduction in GW detectors is pivotal for enhancing the signal detectability as well as the astrophysical outcome. A variety of algorithms, including traditional approaches and those based on machine learning, are now present in the literature for this purpose:

**Wiener filtering**—This is a fundamental filtering technique that is effective when the noise is *stationary* and noise coupling is linear. It aims at minimizing the mean square error (MSE) between estimated and true signals (Wiener 1949; Davis et al. 2019). Its robustness is evident in GW event analysis by the International Gravitational-wave Network (IGWN) (Abbott et al. 2020a). However, its performance becomes sub-optimal for *non-stationary* and *non-linear* noise driven by complex environmental and instrumental fluctuations. This highlights the need for adaptive noise reduction strategies in GW astronomy.

**NonSENS**—Non-Stationary Estimation of Noise Subtraction (NonSENS) employs an Infinite Impulse Response (IIR) filter to remove both stationary and non-stationary noise in GW detectors (Vajente et al. 2020). This method effectively addresses noise arising from slow interferometer movements, such as angular fluctuations, which pose challenges to traditional techniques. By utilizing witness signals to monitor noise and its modulation over time, NonSENS achieves stable, parametric subtraction of *non-stationary* noise. It leverages data science techniques, such as gradient-based optimization (Kingma & Ba 2014), to estimate the coupling coefficients, thereby overcoming the complexities that hinder standard noise reduction methods. Additionally, the analytical filter, with its limited number of coefficients, avoids the computational challenges and interpretability issues often associated with deep neural networks.

**Adaptive Feed-Forward**—The feed-forward technique in Advanced Virgo is designed to mitigate 50 Hz

noise by using a phase signal from the Uninterruptible Power Supply (UPS) as a witness channel. First, the system measures the 50 Hz noise through the UPS. Then, it dynamically adjusts the gain and phase to match the noise observed in the differential arm length (DARM) channel. A 50 Hz resonant filter is applied to isolate and target this specific frequency. Finally, the corrected signal is injected into DARM to cancel out the noise. This adaptive approach continuously adjusts to variations in the noise environment, ensuring efficient and reliable suppression of the 50 Hz disturbance.

### 2.2. DeepClean

Neural networks have emerged as the leading approach for noise reduction due to their adaptability and robustness in managing complex data. These models effectively distinguish between signal and noise, thereby enhancing the overall performance of GW detectors. **DeepClean** uses a CNN architecture to measure the correlation between auxiliary sensors and GW data (Ormiston et al. 2020; Saleem et al. 2023), to mitigate environmental and instrumental noise off the GW data. Figure 1 summarizes the workflow. The architecture features a symmetric one-dimensional auto-encoder with multiple downsampling and upsampling layers, tailored to the sampling frequency and witness channel count. This configuration enables noise prediction across different data dimensions and uses batch normalization and tanh activation functions to boost generalization. The trainable weights of the neural network determine the form of the noise coupling. In the most general case, it can capture *non-linear* couplings by virtue of the non-linear activation functions included in the neural network. With the help of auxiliary sensors tracking the changes in coupling features over time, it can in principle also capture *non-stationary* noise couplings. The training minimizes a loss function based on the noise spectrum ratio of cleaned to original strain across all frequency bins.

The GW strain  $h(t)$  from a detector can be written as follows:

$$h(t) = s(t) + n(t), \quad (1)$$

where  $s(t)$  denotes potential astrophysical signals and  $n(t)$  is the detector noise. The noise can be further decomposed as

$$n(t) = n_R(t) + n_{NR}(t). \quad (2)$$

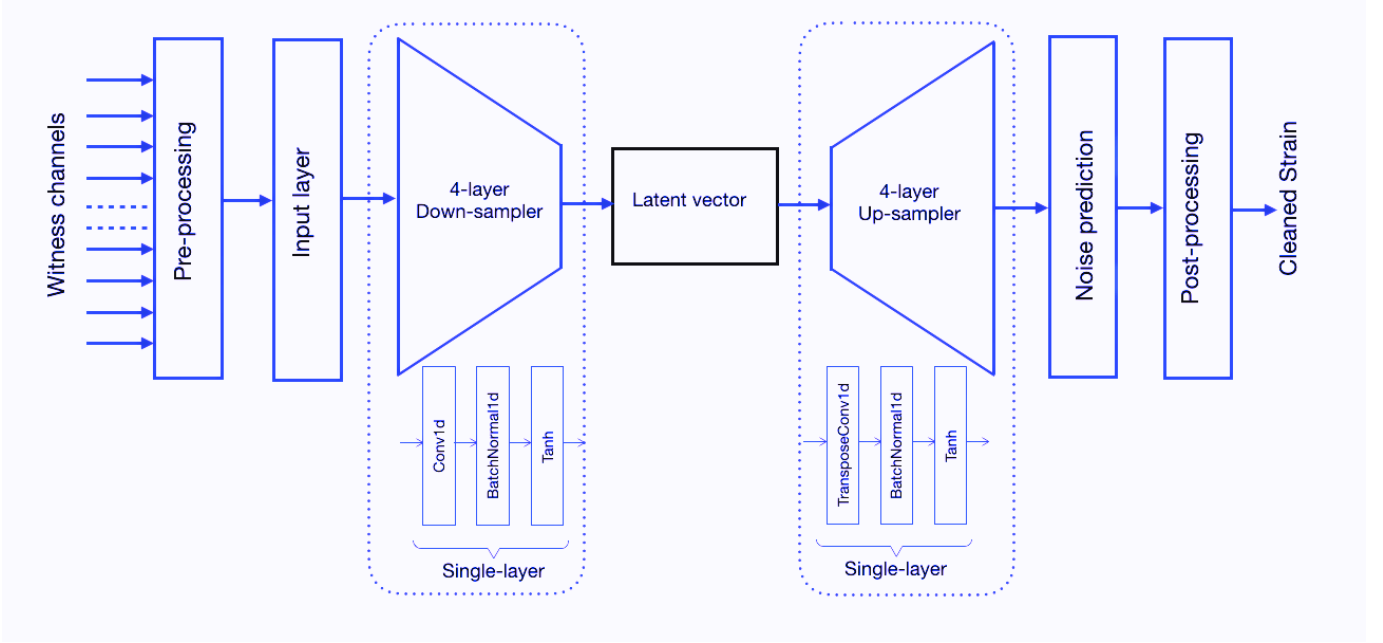


**Figure 1.** Architecture of the **DeepClean** system and the associated data processing sequence. **DeepClean** processes input in the form of time series data acquired from an array of witness sensors. The data undergo a transformation through a convolutional autoencoder network, which consists of a series of four convolutional layers for the reduction of dimensionality, followed by an equal number of transpose-convolutional layers responsible for dimensionality expansion. Each convolutional operation is succeeded by batch normalization and hyperbolic tangent (tanh) activation. The final convolutional layer culminates in a one-dimensional representation aimed at predicting noise.

where  $n_{NR}(t)$  is known as the non-removable noise which are the inherent limitations of the design<sup>1</sup>. On the other hand,  $n_R(t)$  is called the removable noise which is not there in the core design of the interferometers but originates from environmental and technical factors.

The interferometers are equipped with thousands of auxiliary witness channels that record independent instances of noise from various technical and environmental sources and are used to reconstruct the removable noise  $n_R(t)$ . Based on the physical origin, the  $n_R(t)$  can be understood to be a superposition of several noise couplings, schematically written as  $n_R(t) = n_R^{(1)}(t) + n_R^{(2)}(t) + \dots$ , with each term being the result of a unique noise coupling between a unique subset of the witness channels. The denoising efforts with **DeepClean** discussed in this work have to be applied separately on each of those contributions. Our efforts here are to mitigate one or more of the contributors rather than subtracting the entire  $n_R(t)$ , which is beyond the scope of

this work<sup>2</sup>. Henceforth in this paper,  $n_R(t)$  indicates those couplings which we intend to subtract in this work.

A convenient mathematical notation for the **DeepClean** neural network is  $\mathcal{F}(w_k; \vec{\theta})$ , where  $w_k(t)$  represents the data from the witness sensors, and  $\vec{\theta}$  is the set of all the trainable weights of **DeepClean**, which are optimized by minimizing a loss function  $J_{PSD}$ ,

$$\begin{cases} n_R(t) = \mathcal{F}(w_k; \vec{\theta}), \\ \vec{\theta} = \arg\min_{\vec{\theta}'} J_{PSD}[h(t), \mathcal{F}(w_i(t); \vec{\theta}')] \end{cases} \quad (3)$$

Subtracting  $n_R(t, \vec{\theta})$  from the GW strain data  $h(t)$  yields the residual strain  $r(t, \vec{\theta})$  aka cleaned strain.

$$r(t, \vec{\theta}) = h(t) - n_R(t, \vec{\theta}) \quad (4)$$

As mentioned before, the cleaned strain would still contain the non-removable noise, the unknown contributions to the removable noise, and any possible astrophysical signals that are present. The loss function  $J_{PSD}$  is defined as the ratio of the power spectral densities of the

<sup>1</sup> For example, the dependency of thermal noise on the mirror coating material, and the photon shot noise on the laser power used.

<sup>2</sup> Note that there are several frequency bands with unknown noise, which are neither due to design limitations nor associated with known witness channels. Although such noise is included in  $n_R(t)$  and falls under the category of removable noise, it is not currently removable given our present understanding of the available witness channels.

cleaned and raw strain summed over all the frequency bins within the subtraction band,

$$J_{PSD} = \frac{1}{N} \sum_{k=1}^N \frac{PSD_r[k]}{PSD_h[k]}, \quad (5)$$

where  $PSD_h[k]$  represents the power spectral density (PSD) derived from the GW strain data, and  $PSD_r[k]$  represents the PSD of the residual signal,  $r(t)$ . The index  $k$  runs over all the  $N$  frequency bins, uniformly spaced between  $f_{low}$  and  $f_{high}$ . To optimize the weights ( $\theta$ ), **DeepClean** employs the ADAM optimizer, which is an efficient algorithm to minimize the loss function in the gradient space (Kingma & Ba 2014).

### 3. A VIRGO O3B MOCK DATA CHALLENGE

We apply **DeepClean** on Virgo O3b data and assess the performance using various metrics. We examined a continuous stretch of GW strain data `Hrec_hoft_raw_20000Hz` and the useful witness channels, spanning two days, 18 hours and 15 minutes, from February 7, 2020, 16:19:27 UTC to February 10, 2020, 10:35:01 UTC. This period was selected for its extensive coverage and the significant coherence observed between strain and auxiliary channels in the Virgo O3b dataset which is essential for the effective deployment and evaluation of **DeepClean**. The models were trained in 1024s, 2048s, and 4096s segments with the training performed once for every 100,000s of data, after which the model's performance in noise subtraction significantly decreased, necessitating retraining. Each model was used to clean the corresponding segment length. We first focus noise reduction specifically within three frequency bands: 98–110 Hz, 142–162 Hz, and 197–208 Hz. We target these bands due to their excessive noise, which is appropriate for testing the effectiveness of the algorithm and its ability in enhancing the recovery of astrophysical signals in the data. Noise reduction in these bands are particularly interesting in the context of pre-merger detections of Compact Binary Coalescence (CBC) events, especially binary neutron star mergers and other low mass black hole binaries.

#### 3.1. Witness sensors

A comprehensive analysis of witness channels was first performed within the specific frequency bands.

To determine which channels are the most important, we consider the coherence between witness channels and the GW strain channel. We consider the output of the so-called BruCo algorithm (a brute-force coherence computation tool among all channels in Virgo; [Acernese et al. 2023b](#)), which run automatically during the O3b,

to select channels whose coherence exceeded 0.5 (50% of the maximum possible coherence). Additionally, we required that this coherence excess occurred at least five times during February and March 2020. This ensures that each witness channel shows sustained coherence levels across multiple instances. Each witness channel is tested for its noise removal effects and those deemed to not contribute are removed. Below we describe the main witness channels selected for each frequency band.

#### 98 to 110 Hz:

- **V1:CAL\_WE\_MIR\_Z\_NOISE**: Injects and monitors longitudinal noise in the west end mirror for calibration.
- **V1:CAL\_NE\_MIR\_Z\_NOISE**: Injects and monitors longitudinal noise in the North End mirror for calibration.
- **V1:INJ\_IMC\_QD\_FF\_DC\_V**: Measures the DC voltage of the Input Mode Cleaner.

#### 197 to 208 Hz:

- **V1:CAL\_WE\_MIR\_Z\_NOISE**: Injects and monitors longitudinal noise in the west end mirror for calibration.
- **V1:SDB\_EDB\_Tpro\_processed\_packets** and **V1:SDB2\_Tpro\_processed\_packets**: Impacts data quality via suspension database processing.
- **V1:ENV\_IB\_CT\_FINGER\_ACC\_Y**: Monitors environmental vibrations.
- **V1:ENV\_CEB\_MAG\_W**: Monitors magnetic fields and detects magnetic noise.
- **V1:INJ\_IMC\_QD\_FF\_I\_H** and **V1:INJ\_IMC\_REFL\_I\_POST**: Injection Mode Cleaner control signal from the in-phase demodulated quadrant photodiode.
- **V1:SQZ\_CC\_Tpro\_processed\_packets**: Squeezing control system packets.

**142 to 162 Hz**: Given the complex contributions of 167 witness channels in this frequency range to noise reduction, a full listing is omitted. Key acronyms like **ASC** (Alignment Sensing and Control), **INJ** (Injection), **ACT** (Actuation), and **ENV** (Environment) are emphasized to highlight the main systems that maintain the operating integrity of the interferometer ([Acernese](#)



et al. 2023a). The complete list of witness channels can be found here <sup>3</sup>.

### 3.2. Training and cleaning

For each frequency band described above, training is performed independently. What this means is that three separate instances of *DeepClean* are trained, one for each band with the respective set of channels. This leads to three different versions of cleaned strain data with each of them achieving noise reductions in the respective bands. There is no version of cleaned strain with subtraction achieved in all three bands. In a more practical scenario, for a production analysis, training on each band should be performed sequentially, with the cleaned strain output from one band being considered as the unclean input strain for the next band, leading to the final layer giving cleaned strain with noise subtraction achieved in all the considered bands. This has been carried out and described below, with not only three but many more frequency bands and witness channels. For the moment, we focus on the performance in each band separately.

There are a number of hyperparameters which can optimize the performance of *DeepClean*, including the learning rate, kernel size, stride etc. For all of these, we use the same settings as used in Saleem et al. 2023. The data from all the witness channels are first pre-processed such that each timeseries has zero mean and unit variance. These normalized datasets are bandpassed and then divided into overlapping kernels <sup>4</sup>, with kernel size of 8s, and 7.75s overlaps. The 4096s of training data yields 16353 overlapping kernels, calculated using the formula:

$$\begin{aligned} \text{kernels} &= \frac{\text{data duration} - \text{kernel duration}}{\text{shift}} + 1 \\ &= \frac{4096 - 8}{0.25} + 1. \end{aligned}$$

These kernels are then grouped into batches of 32 (known as the `batch_size`), resulting in a total of 512 batches. This implies that during one epoch of training, *DeepClean* iterates and updates the weights 512 times. When the witness channels exhibit moderate to strong coupling, the weights typically converge to their optimal values within 20–30 training epochs. Conversely, if the coupling is absent or very weak, the training may fail to converge or require additional hyperparameter tuning

to achieve meaningful results. Throughout this study, we have used a fixed number of 30 epochs for training. Figure 2 shows the loss in relation to the epochs.

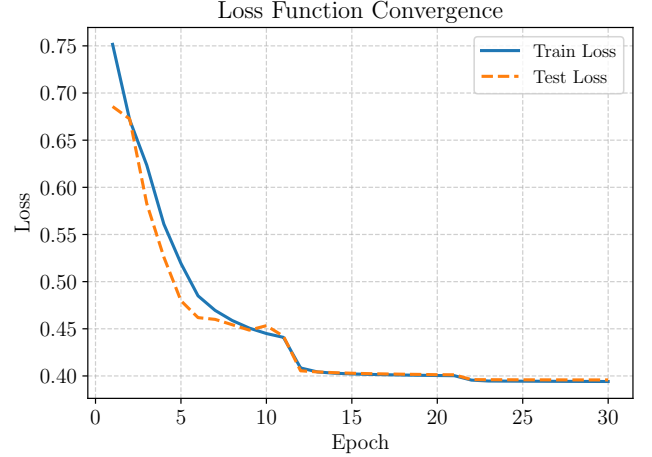


**Figure 2.** The convergence of the loss function during training is shown. The solid blue line represents the training loss, while the dashed orange line indicates the test loss over 30 epochs. Both curves show consistent convergence, demonstrating effective learning and minimal overfitting.

The cleaned strain is produced in chunks of 4096 s for all three bands. In addition to the normalization of the input witness channels mentioned earlier, there are batch normalizations applied at each layer of the neural network to ensure consistent input distributions for the subsequent layers. In *DeepClean*, batch normalization also makes sure that the final noise predictions have nearly zero mean and unit variance. For this reason the predicted noise is subtracted from normalized version of the raw strain, which yields cleaned strain in normalized units. This is then un-normalized with the mean and standard deviation used earlier to normalize the unclean strain. Following that, the cleaned strain is bandpassed to the target frequency band, in order to make sure that *DeepClean* did not make any noise prediction outside the desired frequency band. Hereafter in this paper, *cleaned strain* refers to this post-processed cleaned strain.

## 4. RESULTS

### 4.1. Improvement in the amplitude spectral density (ASD)

#### 4.1.1. Single layer subtractions and their ASD ratio

The primary approach used here for assessing *DeepClean*'s performance is the comparison of the ASD of the cleaned strain (labeled V1:DC) against the original unclean strain (labeled V1:ORG), where V1 denotes

<sup>3</sup> [https://github.com/weizmannk/Virgo-DeepClean/blob/main/config/witnesses/single-layers/witnesses\\_142-162\\_Hz.ini](https://github.com/weizmannk/Virgo-DeepClean/blob/main/config/witnesses/single-layers/witnesses_142-162_Hz.ini)

<sup>4</sup> The kernels are here the segments of data and are distinct from the convolution filter kernels in CNN architecture that carry the weights.

the Virgo detector. Figure 3 illustrates the ASD enhancements for the targeted frequency ranges of 98–110 Hz, 142–162 Hz, and 197–208 Hz. The upper panels in each set of plots display the ASDs, while the lower panels show the ASD ratios of the cleaned strain to the uncleaned strain. Significant subtractions are observed across all three bands. The efficacy of **DeepClean** varied significantly with the length of the training data. Although segments of 1024 s and 2048 s were used, the results were suboptimal compared to those obtained from the 4096 s segments. Figure 3 is produced using a 4096 s segment.

This may be attributed to the non-stationary features in the data during O3b. The data set is characterized by periods in which the auxiliary sensors exhibit high coherence with the readout channel for durations as brief as 200 s, followed by incoherent intervals. Longer training segments, such as 4096 s, are advantageous, as they encompass a broader spectrum of these variable conditions, thereby improving the model’s ability to accurately predict and mitigate them. Consequently, training with 4096 s segments proved to be more effective for O3b Virgo data.

#### 4.1.2. Multi-training and ASD ratio

This section introduces a segmented multi-training approach targeting specific frequency bands that collectively cover the range from 15 to 415 Hz, with each band trained independently.

The multi-training methodology applies a sequential, layer-wise approach. The training and noise cleaning are performed iteratively across frequency bands, with the output of one layer serving as the input for the next, progressively refining noise reduction across the different frequency bands. The process begins with the 142–162 Hz band, selected for its 122 associated witness channels, requiring at least 80 GB of RAM to process 4096 s of Virgo O3b data. This initial layer’s cleaned output forms the basis for subsequent layers.

The full process comprises 13 layers in total: 15–20 Hz, 33–39 Hz, 55–65 Hz, 75–80 Hz, 98–110 Hz, 137–139 Hz, 142–162 Hz, 197–208 Hz, 247–252 Hz, 295–305 Hz, 345–355 Hz, 355–367 Hz, and 395–415 Hz band. Each frequency band is associated with specific witness channels<sup>5</sup> that demonstrate a certain level of coherence. The ASD for the original and cleaned data is presented in Figure 4.

#### 4.2. Improvement of BNS inspiral range

<sup>5</sup> <https://github.com/weizmannk/Virgo-DeepClean/tree/main/config/witnesses/multi-layers>

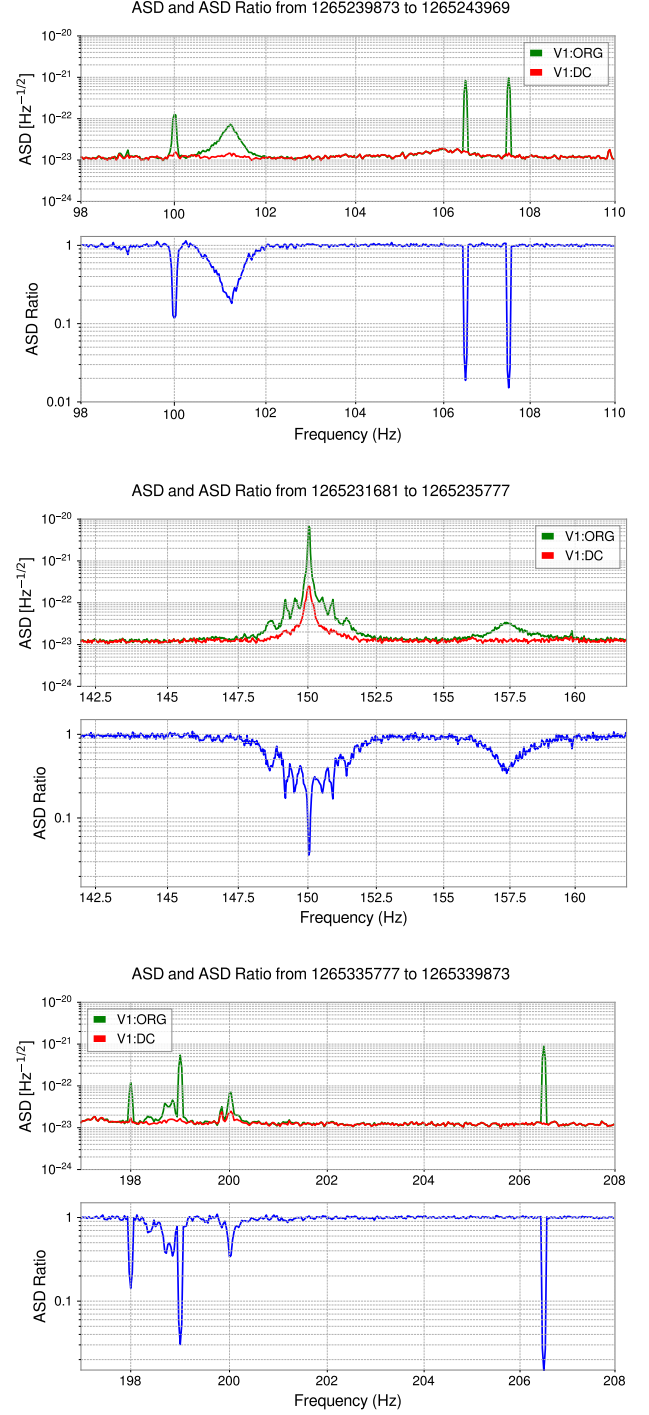


**Figure 3.** ASD and ASD ratio comparison across different frequency bands for Virgo detector data. The green curve represents the ASD of the original data from Virgo (V1:ORG), the red curve depicts the ASD after processing with the **DeepClean** algorithm (V1:DC), and the blue curve shows the ratio of the two ASDs. The top panel demonstrates noise reduction in the 98–110 Hz frequency band, the middle panel in the 142–162 Hz band, and the bottom panel in the 197–208 Hz band. These panels demonstrate the noise reduction capabilities of **DeepClean** within this specific frequency range.

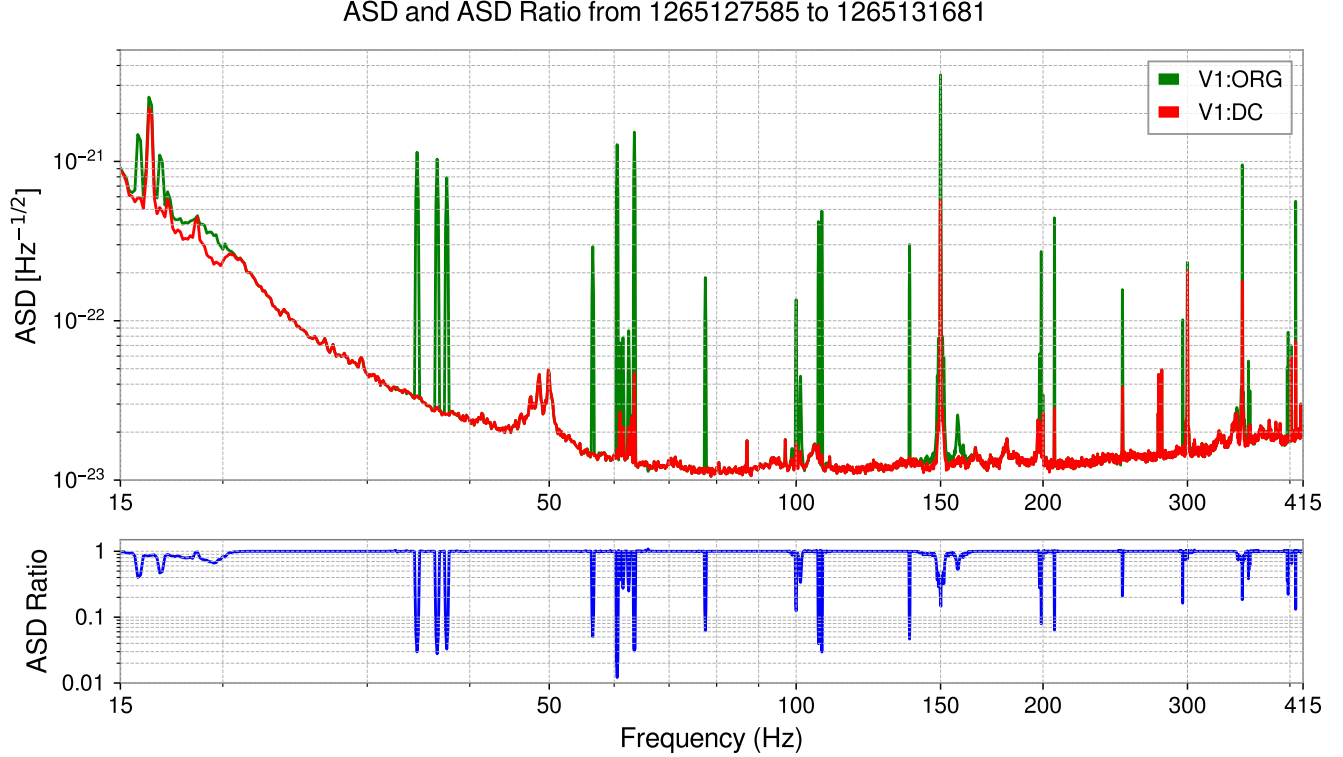


**Figure 4.** Comparison of ASD and ASD ratio across a 15 to 415 Hz frequency band. The original data from Virgo is represented by the green curve (V1:ORG), whereas the red curve (V1:DC) displays the ASD after processing with the **DeepClean** algorithm. The blue curve indicates the ratio of the two ASDs. These visualizations highlight the **DeepClean** algorithm’s noise reduction efficacy across the specified frequency spectrum.

The application of the **DeepClean** algorithm for noise subtraction in GW detectors yields quantifiable improvements in the BNS inspiral range, which is a measure of the average distance at which a binary neutron star (BNS) system with component masses of  $m_1 = m_2 = 1.4 M_\odot$  can be detected with a SNR of 8. This range effectively serves as an indicator of overall GW detector sensitivity (Finn & Chernoff 1993; Chen et al. 2021; Finn 1996). An extended BNS inspiral range reflects heightened detector sensitivity, a direct result of advanced noise reduction methods that enable the capture of fainter, more distant signals.

#### 4.2.1. BNS range from single layer

A comparative analysis conducted before and after implementing **DeepClean** reveals modest yet statistically significant enhancements. Specifically, within the 98–110 Hz band, an average increase of approximately 0.2 Mpc observed, corresponding to an improvement of 0.4%. In the 142–162 Hz band, the average gain approximately 0.19 Mpc or 0.4%. Furthermore, cleaning within the 197–208 Hz band results in a marginal increase of approximately 0.02 Mpc (0.05% improvement).

Figure 5 illustrates the evolution of BNS inspiral range before and after noise subtraction, particularly within the 142–162 Hz band.

This BNS inspiral range shows a daily fluctuation, with maximal values occurring around midnight and at minimal values after 9:00 AM (UTC), driven by local environmental noise sources and site-specific dynamics. These fluctuations primarily stem from changes in anthropogenic noise (e.g., traffic vibrations) and wind conditions (Coughlin et al. 2011; Fiori et al. 2020). Night-time brings optimal sensitivity due to minimal human activity and lower seismic noise, while morning traffic increases ground vibrations, reducing sensitivity.

We will revisit this analysis in a later section, incorporating results from subtraction performed across multiple bands.

#### 4.2.2. BNS range from multi-training

This approach has achieved a significant improvement in the BNS inspiral range, increasing it by approximately 1.3 Mpc, representing a 2.5% enhancement. Similar to the single training case, the contribution of different frequency bands to the inspiral range varies sig-



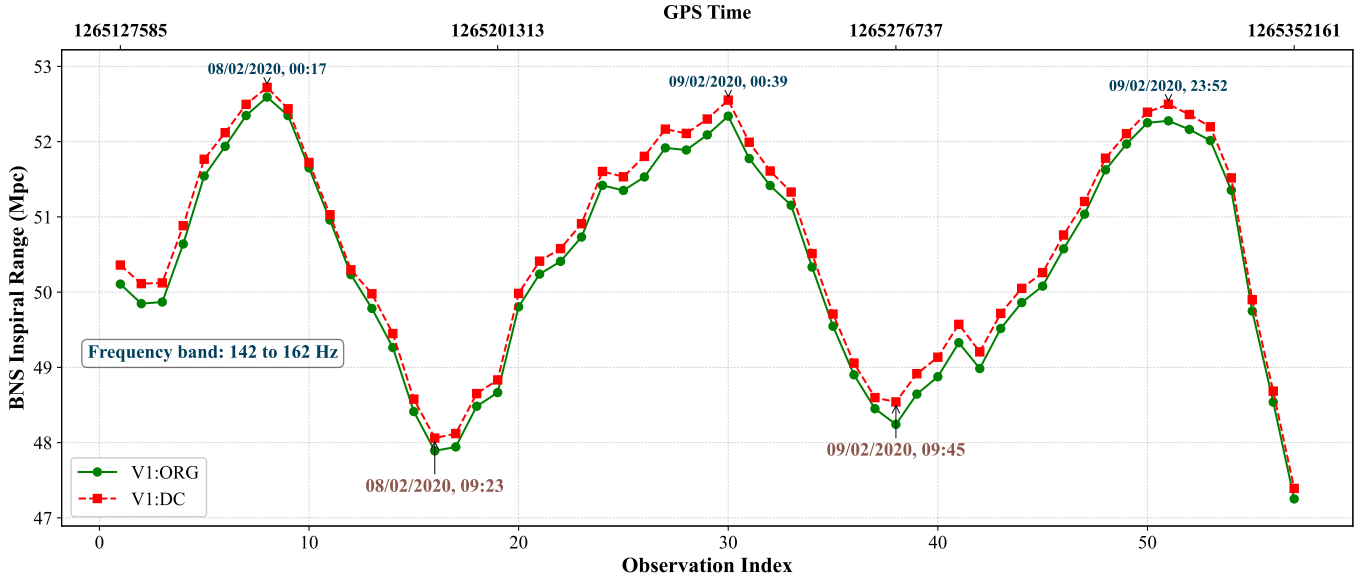


**Figure 5.** Analysis of the inspiral range sensitivity for BNS, using Virgo O3b data from GPS time 1265127585 to 1265352161. The target frequency band for this analysis is the 142–162 Hz range. This plot highlights the **DeepClean** effectiveness in enhancing BNS inspiral detection over each 4096 s segment, represented by the “Observation Index.” Note: The periodic fluctuations reflect anthropogenic noise near the Virgo detector, with the highest sensitivity around midnight and the lowest around 09:00 (UTC), when anthropogenic noise is most prevalent.

nificantly. Some bands contribute substantially, while others have little to no impact. In our analysis, the 55–56 Hz band contributes the most, with an increase of 0.51 Mpc, followed by the 33–39 Hz band, which adds 0.29 Mpc. Frequency bands such as 75–80 Hz, 98–110 Hz, and 142–162 Hz contribute modestly, with increases ranging from 0.12 to 0.17 Mpc. Other bands show minimal or negligible contributions. Figure 6 illustrates the BNS evolution as function of the frequency band (layer index). The results not only reveal the individual contribution of each frequency band but also highlight the importance of this sequential training process. Such a process could significantly enhance the sensitivity of the Virgo detector.

#### 4.3. Performance evaluation using CBC injections

We now conduct an injection analysis using CBC signals. The purpose is to verify that the denoising with *DeepClean* does not alter the GW signals that are present in the data, and also to examine any improvements in the credible intervals of the estimated parameters (Christensen & Meyer 2022).

##### 4.3.1. GW generation and event selection

In the following, we use utilities **LALSuite** and **Bilby** libraries (LIGO Scientific Collaboration et al. 2018; Ashton et al. 2019; Wette 2020) to generate Binary Black hole (BBH) signals. The component masses  $m_1$  and  $m_2$

are drawn from a uniform distribution, ensuring that the total mass  $M$  corresponds to innermost stable circular orbit (ISCO) frequencies  $f_{\text{ISCO}}$  falling within the three targeted frequency bands described above. A similar criterion was employed also by Saleem et al. 2023 for distributing the injection parameters.

The  $f_{\text{ISCO}}$  frequency is defined as,

$$f_{\text{ISCO}} = \frac{c^3}{6^{1.5}\pi GM}, \quad (6)$$

where  $c$  is the speed of light,  $G$  the gravitational constant, and  $M$  the total mass of the binary system.

We inject BBH coalescence signals into the Virgo O3b raw data, referred to as our Mock Data. These injections had ISCO frequencies ranging from  $f_{\text{low}}$  to  $f_{\text{high}}$  and were spaced 32 s apart. The luminosity distances of the signals were uniformly distributed between 5 and 30 Mpc to ensure they were detectable. We apply *DeepClean* to both the original data and the data with injected GW signals.

##### 4.3.2. Signal-to-noise ratio analysis

Following the procedure described in Section 4.3.1, we inject a total of 3,200 GW signals from BBH mergers into the dataset, spanning the full frequency range of 15–415 Hz. The SNR of each injected signal was computed using the matched-filter function provided by *PyCBC* (Bier et al. 2019), with a waveform template corresponding to the injected signal.

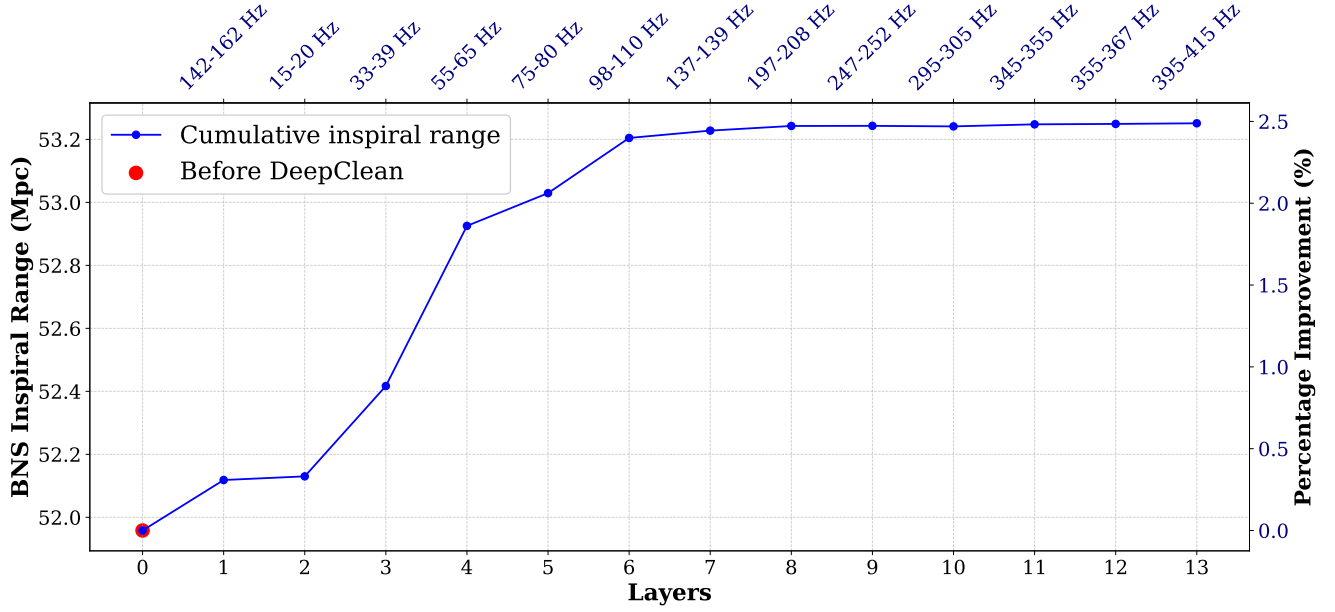


**Figure 6.** Cumulative BNS inspiral range (blue curve) as a function of sequential training layers in the **DeepClean** algorithm, covering the frequency band from 15 to 415 Hz. Each layer corresponds to a distinct frequency band, starting with the 142–162 Hz band. Subsequent layers are trained iteratively, building upon the output of the preceding layer. The red marker represents the baseline inspiral range before applying **DeepClean**.

For each injection, the matched-filter SNR was calculated both before and after applying **DeepClean**.

The difference in SNR is determined as the fractional change,  $\frac{\Delta \text{SNR}}{\text{SNR}}$ , where a positive value indicates a gain. Figure 8 shows the distribution of fractional SNR differences for the 98–110 Hz and 142–162 Hz bands, while Figure 7 displays the SNR fractional difference from multi-band subtraction over the full range of 15–415 Hz. We observe that some injections exhibit an SNR gain, while others show a loss. This variability is expected due to the stochastic nature of the noise prediction by **DeepClean**, which can influence the matched-filter SNR in either direction. However, the PSD consistently improves after applying **DeepClean**, contributing positively to SNR enhancement. The net effect on SNR arises from the combination of PSD improvement and the random nature of noise prediction, determining whether an injection experiences a gain or loss.

While single-band subtractions do not consistently yield a clear SNR gain—with approximately equal numbers of injections gaining and losing SNR—multi-band subtraction shows a significant improvement, with over 70% of injections recording an SNR gain.

To analyze these results further, we categorized the SNR fractional differences into three groups based on a threshold: unchanged ( $|\frac{\Delta \text{SNR}}{\text{SNR}}| \leq 1\%$ ), increased ( $\frac{\Delta \text{SNR}}{\text{SNR}} > 1\%$ ), and decreased ( $\frac{\Delta \text{SNR}}{\text{SNR}} < -1\%$ ). For multi-band subtraction, 71.3% of GW signals showed an increase, 28.5% showed a decrease, and only 0.2%

remained unchanged. For the three single bands—98–110 Hz, 142–162 Hz, and 197–208 Hz—the percentages of injections with SNR gains were 74.8%, 45.3%, and 48.8%, respectively. The remainder in each band either experienced a decrease or remained unchanged (with only 0.2–3.2% unchanged per band).

Table 1 provides the mean and standard deviations of the SNR fractional difference distributions. The final column includes the  $1\sigma$  credible intervals for percentage differences. For multi-band subtraction, the  $1\sigma$  credible interval indicates that the change in SNR after **DeepClean** relative to the original SNR lies between -2.4% and 5.9%. The upper bound clearly demonstrates a dominance of SNR gains over losses. For single-band subtractions, as noted earlier, no clear dominance in SNR gain is observed.

#### 4.3.3. Parameter Estimation: Testing **DeepClean**’s Impact on GW Signal structure

In this section, we describe a parameter estimation study to confirm that **DeepClean** does not adversely affect the astrophysical signals present in the data. We injected 128 BBH coalescence signals with ISCO frequencies ranging from 15 to 415 Hz, over a 4096 s interval starting at GPS time 1265127585. For a BBH signal, at least 15 independent parameters need to be estimated simultaneously. In this study, we adopt a *one-at-a-time* approach, estimating a single parameter of interest while fixing all other parameters to their true or injected val-

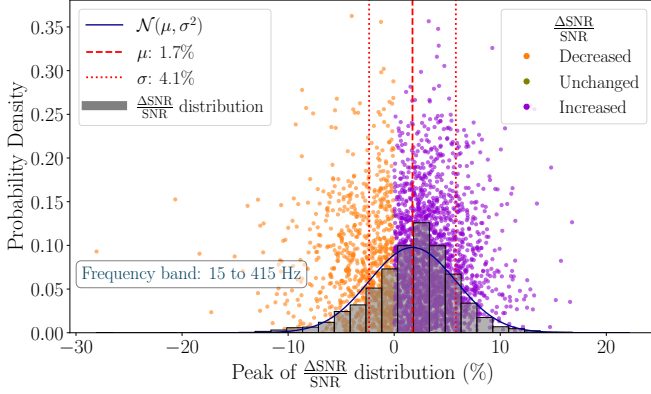


**Figure 7.** The figure illustrates the probability density distribution of the relative change in SNR, defined as  $\frac{\Delta \text{SNR}}{\text{SNR}}$ , for signal injections across the 15–415 Hz frequency band. This compares the SNR values before and after applying DeepClean. The histogram bars represent the distribution of the relative change in SNR, with a Gaussian fit overlaid. The key statistics, including the mean ( $\mu = 1.7\%$ ) and standard deviation ( $\sigma = 4.1\%$ ), are highlighted. Individual points depict changes in SNR for each injection and are categorized as decreased, unchanged, or increased.

**Table 1.** Statistical analysis of SNR fractional differences over frequency bands.

Frequency band	$\mu$ (%)	$\sigma$ (%)	(%) $\frac{\Delta \text{SNR}}{\text{SNR}}$ at $1\sigma$
Single training			
98–110 Hz	0.8	1.4	-0.62%–2.15%
142–162 Hz	-0.3	2.7	-3.05%–2.42%
197–208 Hz	0	0.4	-0.35%–0.36%
Multi-training			
15–415 Hz	1.7	4.1	-2.36%–5.81%

ues. This approach allows us to isolate and analyze the effects on individual parameters more effectively.

A parameter estimation validation study typically serves two purposes. The first and most critical goal is to test whether the signal retains its original structure after noise regression, which would manifest as biases in the estimated parameters. The second goal is to evaluate any improvement in the uncertainty of the estimated parameters resulting from noise removal. For the former, the *one-at-a-time* approach is particularly suitable because the full 15-dimensional parameter space, with its inherent degeneracies, may mask subtle biases by redistributing them among degenerate parameters. For example, if the bandpass filters used in DeepClean introduce additional phase to the signal, this

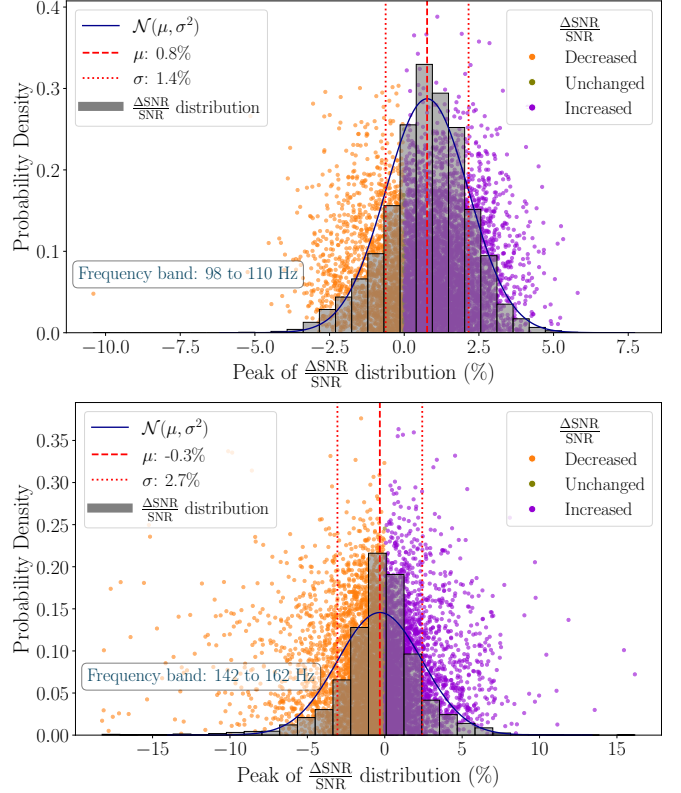


**Figure 8.** The **top panel** illustrates the distribution of the relative change in SNR ( $\frac{\Delta \text{SNR}}{\text{SNR}}$ ) for injections in the 98–110 Hz frequency band before and after applying DeepClean. The gray bars represent the probability density of the relative change in SNR, while the solid line shows a Gaussian fit. The mean ( $\mu = 0.8\%$ ) and standard deviation ( $\sigma = 1.4\%$ ) are indicated with red dashed and dotted lines, respectively. The scatter points represent individual values of the relative change in SNR: orange for decreased, green for unchanged, and violet for increased. The **bottom panel** presents the same analysis for the 142–162 Hz frequency band. The mean ( $\mu = -0.3\%$ ) and standard deviation  $\sigma = 2.7$  are similarly indicated. These figures emphasize the variability and statistical consistency of  $\frac{\Delta \text{SNR}}{\text{SNR}}$  after applying DeepClean across different frequency bands, with clear categorization of the changes.

would bias the coalescence phase parameter. However, such a bias could be reabsorbed into other parameters, such as the time of arrival or the sky location of the source. By fixing all other parameters to their true values, we eliminate the possibility of such reabsorption, ensuring that any additional phase is directly captured as a bias. Without the *one-at-a-time* approach, a full 15-dimensional parameter estimation would be necessary to obtain realistic uncertainty estimates. Since the focus of this study is on preserving the signal structure, we exclusively rely on the *one-at-a-time* method, which is also computationally much less demanding.

In Figure 9, we present example posterior distributions for the chirp mass  $\mathcal{M}c$ , mass ratio  $q$ , component spin magnitudes  $a_1$  and  $a_2$ , inclination angle  $\theta_{jn}$ , and luminosity distance  $d_L$  for one representative injection (injection 24). The blue solid and orange dashed curves represent the posterior distributions obtained from the uncleaned and **DeepClean** strains, respectively, while vertical dashed lines indicate the injected (true) parameter values. We observe that the posterior peaks derived from the uncleaned strain exhibit slight offsets from the injected values due to the random nature of noise. In contrast, posteriors from the **DeepClean** strain align more accurately with both the injected and zero-noise values, demonstrating reduced bias. For comparison, the green dotted curves represent posteriors obtained from the same injection but without noise.

Figure 10 presents probability-probability (PP) plots constructed from the full set of 128 BBH injections. These plots illustrate the fraction of injections recovered (y-axis) within a specified credible interval (x-axis). The results from **DeepClean** closely follow the diagonal reference line and lie within the expected confidence intervals, confirming well-calibrated and unbiased parameter recovery. This indicates that **DeepClean** successfully reduces noise without introducing systematic artifacts into the strain.

However, the PP plots from the uncleaned data show clear deviations, notably falling below the diagonal for parameters such as  $\theta_{jn}$ , and  $d_L$ . These deviations indicate biases caused by non-Gaussian noise. These findings underscore that the application of **DeepClean** with a multi-training approach not only efficiently reduces residual noise over a wide frequency range but also preserves gravitational-wave signal integrity and decreases uncertainties in parameter measurements. These frequency-sensitive parameters also show slight reductions in posterior uncertainties, as illustrated by the narrower posterior distributions in Figure 9.

## 5. SUMMARY AND CONCLUSIONS

One of the main challenges faced by noise regression pipelines such as *DeepClean* is the large number of witness channels available, many of which exhibit non-negligible coherence with the strain channel. Handling more than a few tens of channels exceeds our computational capacity, even with state-of-the-art resources (Reissel et al. 2025). In this paper, we demonstrate that identifying and dividing the channels into smaller frequency bands achieves significant success in noise subtraction. *DeepClean*, previously demonstrated with the two LIGO detectors, showcases its capability for non-linear noise regression in Virgo, a detector with distinct

design features, thereby highlighting its generality. Additionally, we employ a computationally efficient alternative for validating the subtraction by using a *one-at-a-time* parameter estimation approach.

In this study of the **DeepClean** framework applied to the Virgo detector data, we demonstrated an increase in sensitivity of the Virgo detector, improving the detection prospects for GW signals. The results are promising and we expect the method can be used in the ongoing O4b campaign for noise reduction. In the future, there are a number of challenges we plan to tackle:

- **Online analysis:** All analysis in this paper was performed offline, however, online processing will be critical to take advantage of the noise improvements in O5, enhancing real-time noise reduction in the Virgo detector and improving pre-merger GW signal detection.
- **High computational demands:** Analyzing Virgo data to capture the 150 Hz peak and its sidebands via ASC witness sensors required significant computational resources, often compromising between data depth and computing power, and we will explore alternative architectures that may be more memory efficient.
- **Data access:** To address these high computational demands, the VirgoTool Python package<sup>6</sup> was identified as a potential solution for reducing data reading times. However, integration challenges within our cluster’s environment limited its utility. We suggest enhancing the gwpy library with VirgoTool’s data handling capabilities to improve computational efficiency in future studies.

## 6. ACKNOWLEDGEMENTS

R.W.K were supported by the Axe “ondes gravitationnelles/multimessager” de l’Observatoire de la Côte d’Azur, Boulevard de l’Observatoire, F-06304 Nice. M.S. and M.W.C acknowledge the support from the National Science Foundation with grant numbers PHY-2308862 and PHY-2117997.

The authors are very grateful to Alba Romero Rodríguez for her review on behalf of Virgo DRS and P&P, which has been useful in the improving of this paper. We would also like to thank Nathalie Besson for her valuable feedback, which enhanced the clarity and precision of the manuscript.

The authors acknowledge the IGWN Computing Grid (CIT, LHO, LLO) for providing resources to realize

<sup>6</sup> <https://anaconda.org/conda-forge/pythonvirgotools>

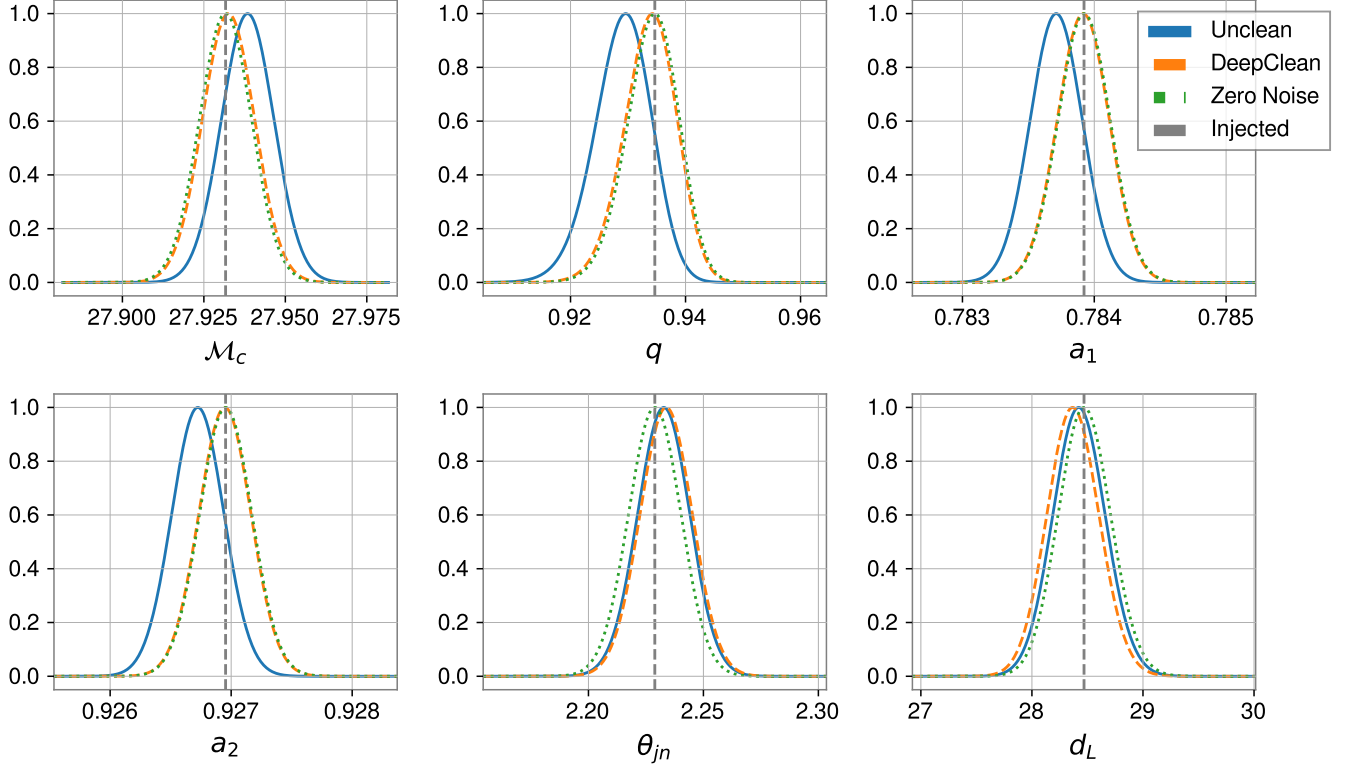


**Figure 9.** The posteriors of single-parameter PE (parameter estimation) of one of the 128 injections. The solid (blue) posterior is from the unclean data, the dashed (orange) posterior corresponds to the data after applying *DeepClean*. The injected values are shown in dashed vertical lines (grey). The unclean data yields posteriors peaking away from the true values, which may be attributed to the particular noise realization together with the non-Gaussian artifacts present in the noise. While the *DeepClean* processed data yield posteriors that closely align with the injected values, illustrating reduced noise-induced bias. For sanity of the analysis, we also show the posterior signal with no noise realization (referred to as *zero-noise*) which peaks at the injected values as expected.

our simulations. We acknowledge the Virgo DetChar and Virgo cluster at Cascina for providing resources that contributed to the research results reported within this paper. This research used resources of the National Energy Research Scientific Computing Center (NERSC), a U.S. Department of Energy Office of Science User Facility operated under contract No. DE-AC02-05CH11231 under project “Toward a complete catalog of variable sources to support efficient searches

for compact binary mergers and their products.” This work used the Advanced Cyberinfrastructure Coordination Ecosystem: Services & Support (ACCESS). This work used the Extreme Science and Engineering Discovery Environment (XSEDE) COMET at SDSU through allocation AST200016 and AST200029. This material is based upon work supported by NSF’s LIGO Laboratory, which is a major facility fully funded by the National Science Foundation

## REFERENCES

- Abbott, B. P., Abbott, R., Collaboration, T. L. S., & the Virgo Collaboration. 2020a, *Classical and Quantum Gravity*, 37, 055002, doi: [10.1088/1361-6382/ab685e](https://doi.org/10.1088/1361-6382/ab685e)
- Abbott, B. P., Abbott, R., Abbott, T. D., et al. 2017, *Phys. Rev. Lett.*, 119, 161101, doi: [10.1103/PhysRevLett.119.161101](https://doi.org/10.1103/PhysRevLett.119.161101)
- . 2020b, *The Astrophysical Journal*, 892, L3, doi: [10.3847/2041-8213/ab75f5](https://doi.org/10.3847/2041-8213/ab75f5)
- Abbott, R., Abbott, T. D., Acernese, F., et al. 2023, *Phys. Rev. X*, 13, 011048, doi: [10.1103/PhysRevX.13.011048](https://doi.org/10.1103/PhysRevX.13.011048)
- Abbott, R., Abbott, T. D., Abraham, S., et al. 2021a, *Phys. Rev. X*, 11, 021053, doi: [10.1103/PhysRevX.11.021053](https://doi.org/10.1103/PhysRevX.11.021053)
- Abbott, R., et al. 2021b, *Phys. Rev. D*, 104, 022004, doi: [10.1103/PhysRevD.104.022004](https://doi.org/10.1103/PhysRevD.104.022004)
- Abbott et al. 2016, *Phys. Rev. Lett.*, 116, 241103, doi: [10.1103/PhysRevLett.116.241103](https://doi.org/10.1103/PhysRevLett.116.241103)



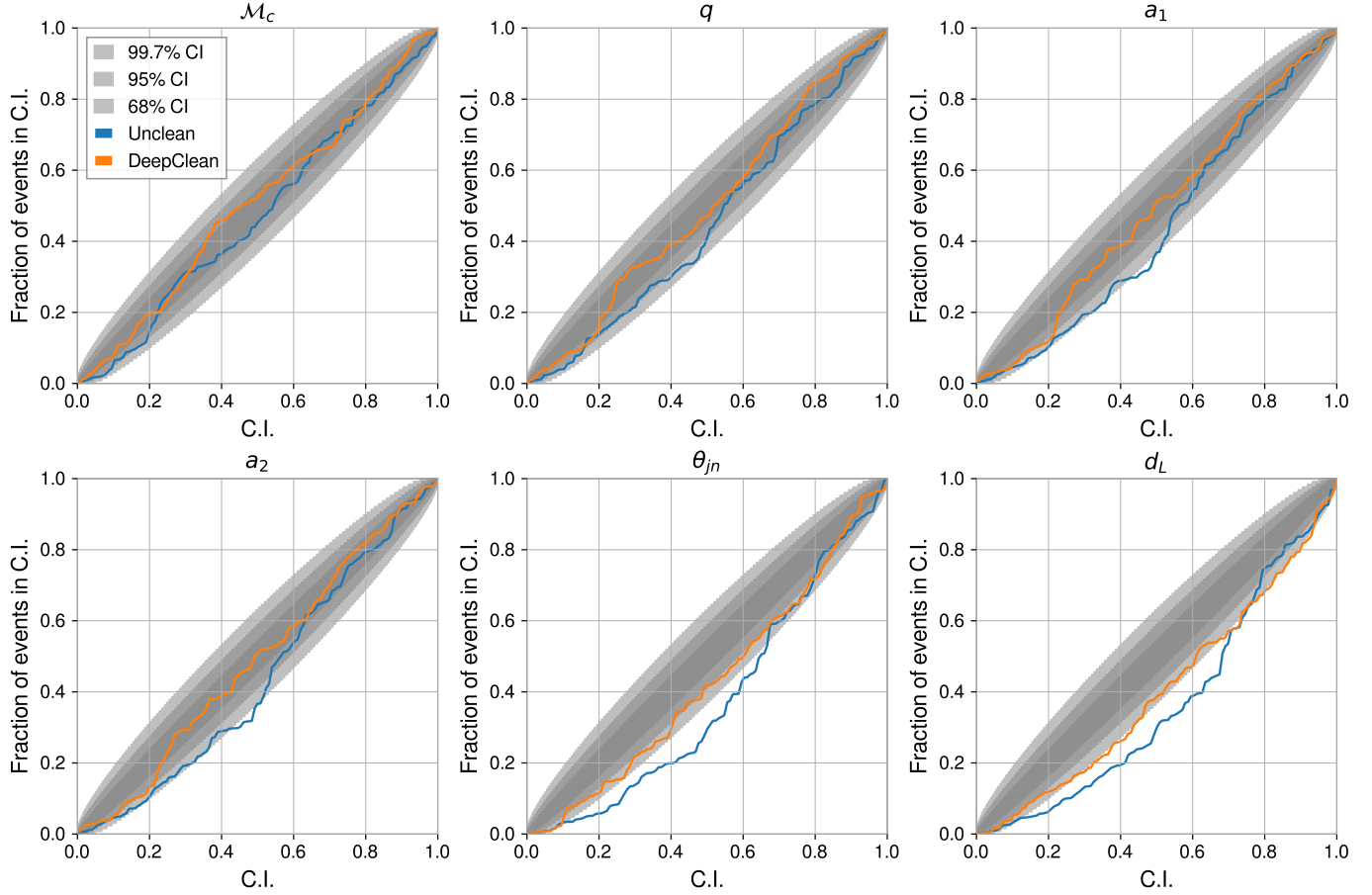


**Figure 10.** The PP plots of the six parameters with unclean and **DeepClean** strain showing that **DeepClean** does not affect the recovery of the underlying physical parameters.

Acernese, F., Agathos, M., Agatsuma, K., et al. 2014, *Classical and Quantum Gravity*, 32, 024001, doi: [10.1088/0264-9381/32/2/024001](https://doi.org/10.1088/0264-9381/32/2/024001)

Acernese, F., Agathos, M., Ain, A., et al. 2023a, *Classical and Quantum Gravity*, 40, 185006, doi: [10.1088/1361-6382/acdf92d](https://doi.org/10.1088/1361-6382/acdf92d)

—. 2023b, *Classical and Quantum Gravity*, 40, 185005, doi: [10.1088/1361-6382/acdf36](https://doi.org/10.1088/1361-6382/acdf36)

Allocca, A., Bersanetti, D., Casanueva Diaz, J., et al. 2020a, *Galaxies*, 8, doi: [10.3390/galaxies8040085](https://doi.org/10.3390/galaxies8040085)

—. 2020b, *Galaxies*, 8, doi: [10.3390/galaxies8040085](https://doi.org/10.3390/galaxies8040085)

Ashton, G., et al. 2019, *Astrophys. J. Suppl.*, 241, 27, doi: [10.3847/1538-4365/ab06fc](https://doi.org/10.3847/1538-4365/ab06fc)

Biwer, C. M., Capano, C. D., De, S., et al. 2019, *Publ. Astron. Soc. Pac.*, 131, 024503, doi: [10.1088/1538-3873/aaef0b](https://doi.org/10.1088/1538-3873/aaef0b)

Buikema, A., Cahillane, C., Mansell, G. L., et al. 2020, *Phys. Rev. D*, 102, 062003, doi: [10.1103/PhysRevD.102.062003](https://doi.org/10.1103/PhysRevD.102.062003)

Chen, H.-Y., Holz, D. E., Miller, J., et al. 2021, *Classical and Quantum Gravity*, 38, 055010, doi: [10.1088/1361-6382/abd594](https://doi.org/10.1088/1361-6382/abd594)

Christensen, N. 2018, *Reports on Progress in Physics*, 82, 016903, doi: [10.1088/1361-6633/aae6b5](https://doi.org/10.1088/1361-6633/aae6b5)

Christensen, N., & Meyer, R. 2022, *Rev. Mod. Phys.*, 94, 025001, doi: [10.1103/RevModPhys.94.025001](https://doi.org/10.1103/RevModPhys.94.025001)

Coughlin, M. W., (for the LIGO Scientific Collaboration, & the Virgo Collaboration). 2011, *Classical and Quantum Gravity*, 28, 235008, doi: [10.1088/0264-9381/28/23/235008](https://doi.org/10.1088/0264-9381/28/23/235008)

Davis, D., Massinger, T., Lundgren, A., et al. 2019, *Classical and Quantum Gravity*, 36, 055011, doi: [10.1088/1361-6382/ab01c5](https://doi.org/10.1088/1361-6382/ab01c5)

Driggers, J. C., Vitale, S., Lundgren, A. P., et al. 2019, *Phys. Rev. D*, 99, 042001, doi: [10.1103/PhysRevD.99.042001](https://doi.org/10.1103/PhysRevD.99.042001)

Finn, L. S. 1996, *Phys. Rev. D*, 53, 2878, doi: [10.1103/PhysRevD.53.2878](https://doi.org/10.1103/PhysRevD.53.2878)

Finn, L. S., & Chernoff, D. F. 1993, *Phys. Rev. D*, 47, 2198, doi: [10.1103/PhysRevD.47.2198](https://doi.org/10.1103/PhysRevD.47.2198)

- Fiori, I., Paoletti, F., Tringali, M. C., et al. 2020, *Galaxies*, 8, doi: [10.3390/galaxies8040082](https://doi.org/10.3390/galaxies8040082)
- Kiendrebeogo, R. W., Farah, A. M., Foley, E. M., et al. 2023, *The Astrophysical Journal*, 958, 158, doi: [10.3847/1538-4357/acfcbl](https://doi.org/10.3847/1538-4357/acfcbl)
- Kingma, D. P., & Ba, J. 2014, arXiv e-prints, arXiv:1412.6980, doi: [10.48550/arXiv.1412.6980](https://doi.org/10.48550/arXiv.1412.6980)
- LIGO Scientific Collaboration, Virgo Collaboration, & KAGRA Collaboration. 2018, LVK Algorithm Library - LALSuite, Free software (GPL), doi: [10.7935/GT1W-FZ16](https://doi.org/10.7935/GT1W-FZ16)
- LSC, Aasi, J., Abbott, B. P., et al. 2015, *Classical and Quantum Gravity*, 32, 074001, doi: [10.1088/0264-9381/32/7/074001](https://doi.org/10.1088/0264-9381/32/7/074001)
- Martynov, D. V., Hall, E. D., Abbott, B. P., et al. 2016, *PhRvD*, 93, 112004, doi: [10.1103/PhysRevD.93.112004](https://doi.org/10.1103/PhysRevD.93.112004)
- Ormiston, R., Nguyen, T., Coughlin, M., Adhikari, R. X., & Katsavounidis, E. 2020, *Phys. Rev. Res.*, 2, 033066, doi: [10.1103/PhysRevResearch.2.033066](https://doi.org/10.1103/PhysRevResearch.2.033066)
- Petrov, P., Singer, L. P., Coughlin, M. W., et al. 2022, *The Astrophysical Journal*, 924, 54, doi: [10.3847/1538-4357/ac366d](https://doi.org/10.3847/1538-4357/ac366d)
- Reissel, C., Soni, S., Saleem, M., et al. 2025, Coherence DeepClean: Toward autonomous denoising of gravitational-wave detector data. <https://arxiv.org/abs/2501.04883>
- Saleem, M., Gunny, A., Chou, C.-J., et al. 2023, Demonstration of Machine Learning-assisted real-time noise regression in gravitational wave detectors. <https://arxiv.org/abs/2306.11366>
- Vajente, G., Huang, Y., Isi, M., et al. 2020, *Phys. Rev. D*, 101, 042003, doi: [10.1103/PhysRevD.101.042003](https://doi.org/10.1103/PhysRevD.101.042003)
- Wette, K. 2020, *SoftwareX*, 12, 100634, doi: [10.1016/j.softx.2020.100634](https://doi.org/10.1016/j.softx.2020.100634)
- Wiener, N. 1949, *Extrapolation, Interpolation, and Smoothing of Stationary Time Series, with Engineering Applications* (The MIT Press). <https://api.semanticscholar.org/CorpusID:125829144>